

## Supplementary Materials for

### **Ultrafast low-energy electron diffraction in transmission resolves polymer/graphene superstructure dynamics**

Max Gulde, Simon Schweda, Gero Storeck, Manisankar Maiti, Hak Ki Yu,  
Alec M. Wodtke, Sascha Schäfer, Claus Ropers\*

\*Corresponding author. E-mail: [cropers@gwdg.de](mailto:cropers@gwdg.de)

Published 11 July 2014, *Science* **344**, 200 (2014)

DOI: 10.1126/science.1250658

#### **This PDF file includes:**

Materials and Methods

Figs. S1 to S8

References

## Materials and Methods

### Sample Preparation

Monolayer graphene is grown in a chemical vapor deposition (CVD) process (37) on 25  $\mu\text{m}$  thick Cu foil (Alfa Aesar, 99.8 % purity). A typical growth process consists of the following steps: (i) Evacuation of the quartz tube reaction chamber to about 3 mTorr. (ii) Introduction of a 40 sccm flow of hydrogen gas at a pressure of 950 mTorr. (iii) Heating of the Cu foil to 1000° C over a period of 60 min and subsequent annealing for 30 min to enlarge the Cu grains and remove residual Cu oxide and impurities. (iv) Introduction of a 6 sccm flow of methane gas with 20 sccm hydrogen into the chamber for 10 min with a total pressure of 460 mTorr for the graphene synthesis. (v) Rapid cool-down of the furnace to room temperature under a 20 sccm flow of hydrogen. The growth of monolayer graphene was verified by Raman spectroscopy.

For graphene transfer, one side of the graphene/Cu foil is covered with a thin layer of poly(methyl methacrylate) (PMMA) by spin coating at 2000 rpm for 60 s, and is dried under atmospheric conditions for 1 h (PMMA vendor and properties: Allresist, molecular weight: 950,000 g/mol, polydispersity index: 3.76, glass temperature: 105° C, melting temperature: 130° C - 160° C, dissolved in ethyl lactate, solid content: 4.0 %).

Subsequently, the uncoated (polymer-free) side of the graphene sample is etched in an oxygen plasma for 30 s at 100 W to remove backside graphene. After etching the Cu foil in a  $(\text{NH}_4)_2\text{S}_2\text{O}_8$  solution (0.3 M) for 6 h, the floating graphene/PMMA film is washed in several cycles with deionized (DI) water. The resulting graphene/PMMA film is then transferred onto transmission electron microscopy (TEM) grids (400 mesh copper grid, covered with Quantifoil film with 3.5  $\mu\text{m}$  hole size). Drying the sample for an extended period of time (3 days) enhances the adhesion of the graphene to the TEM grid. Most of the PMMA, except for that directly in contact with the graphene, is removed by consecutively dissolving it in acetone, isopropanol, and DI (for 15 min each). Figure S3 shows a high-resolution TEM image of the PMMA/graphene bilayer system.

The polymer superstructure was prepared on several dozen samples, and it has proven to be resistant to both thermal treatment and various organic solvents (32, 38). In contrast, the superstructure is sensitive to excessive electron beam irradiation due to PMMA chain damage, highlighting the importance of the present low-dose experiment for its observation (39, 40).

### Estimate for temperature increase at fluence threshold

In order to estimate the temperature increase of the graphene at the fluence threshold of 3  $\text{mJ/cm}^2$ , the following assumptions are made: The pulse energy is deposited only in the graphene (absorption 2.3%, see Ref. (41)), whereas the PMMA is transparent at the pump wavelength of 800 nm. The specific heat capacity  $c_G$  of graphene equals that of graphite for  $T > 100$  K (42) and can be approximated (with temperature  $T$  in Kelvin) as

$$c_G = 9 \cdot 10^{-16}T^6 - 6 \cdot 10^{-12}T^5 + 2 \cdot 10^{-8}T^4 + 0.0092T^2 + 0.946T - 10.481 \text{ (J/kgK)}$$

between 200 K and 1200 K (43), leading to an initial graphene lattice temperature increase of 541 K.

The subsequent PMMA temperature increase of about 145 K at the fluence threshold was estimated using the measured expansion (1%) and a thermal expansion coefficient of  $\alpha = 70 \cdot 10^{-6} \text{K}^{-1}$  (44).

#### Thermal boundary resistance (Kapitza resistance)

The thermal boundary resistance  $R_K = \sigma_K^{-1}$  can be estimated considering the energy flux across the PMMA/graphene interface to be of the form (45)

$$c_{PMMA}\rho d \frac{\partial T_f(t)}{\partial t} = -\sigma_K [T_f(t) - T_s(t)]$$

with  $c_{PMMA}$  the specific heat capacity,  $d$  the film thickness,  $\sigma_K$  the thermal boundary conductance,  $\rho$  the mass density of PMMA, and  $T_f$  and  $T_s$  as the film and substrate temperatures, respectively. From this, assuming approximately temperature-independent material constants, the thermal boundary resistance can be extracted as

$$R_K = \frac{\tau}{c_{PMMA}d\rho}.$$

Using the specific heat capacity  $c_{PMMA} = 1466 \text{ J/kg K}$  and mass density  $\rho = 1.18 \text{ g/cm}^3$  of bulk PMMA, respectively, the experimentally obtained temporal decay time of  $\tau = 43 \text{ ps}$  (Fig. S1), and assuming a film thickness of  $d = 5 \text{ \AA}$ , we extract a value of about  $R_K = 5 \cdot 10^{-8} \text{ m}^2 \text{ K/W}$ , which is close to reported values for similar systems ( $R_K = 8 \cdot 10^{-8} \text{ m}^2 \text{ K/W}$ , see Refs. (46, 47)).

#### Radial diffraction intensity for isotropic and six-fold symmetric components

The decomposition of the diffraction intensity in an isotropic and a sixfold-symmetric component is depicted in Fig. S2.

Starting from a difference image (Fig. S2A), the radial diffraction intensity is computed by averaging over azimuthal angles  $\phi$  around the symmetry center of the diffraction pattern for a given radius  $r$ . Figure S2B shows the regions which are averaged to extract the isotropic component of the diffraction image. The six-fold symmetric diffraction component is obtained by subtracting the previously computed isotropic component from the average over the regions indicated in Fig. S2C.

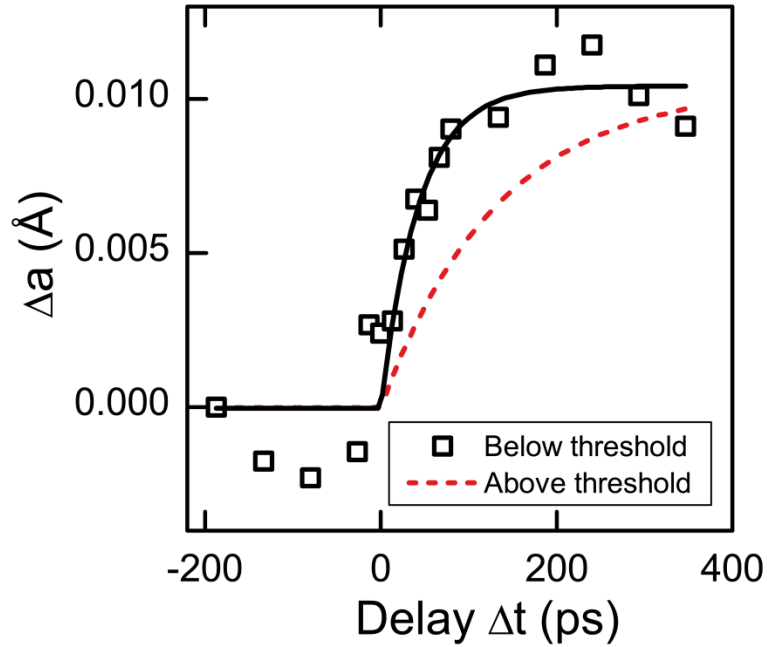


**Fig. S1.** Expansion of crystalline PMMA component above and below the fluence threshold for superstructure melting. Delay-dependent change in PMMA chain-spacing (black squares) for a pump fluence of  $1.9 \text{ mJ/cm}^2$  (below the threshold fluence of  $3 \text{ mJ/cm}^2$ ). An exponential fit (solid black line) yields a time constant of  $\tau = 43 \text{ ps}$ . For comparison, the same fit is plotted with  $\tau = 133 \text{ ps}$  (dashed red line), as found for a pump fluence of  $6 \text{ mJ/cm}^2$  (above the melting threshold, Fig. 4B).

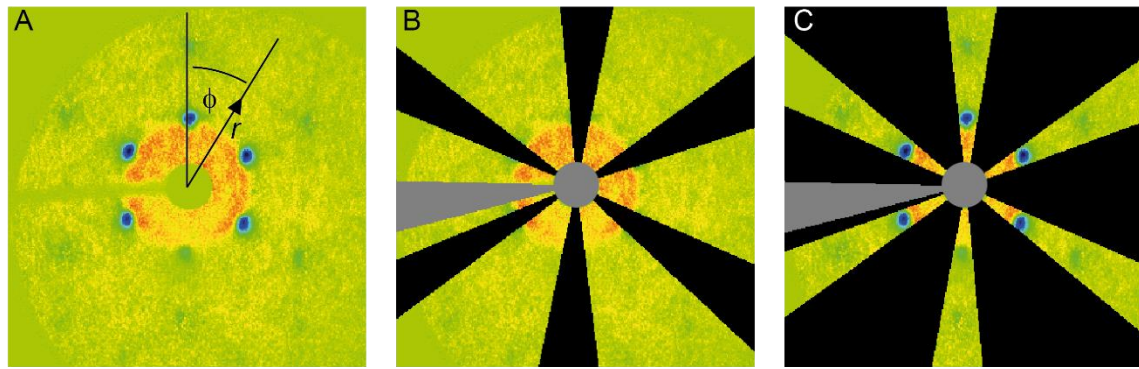


**Fig. S2.** Isotropic and six-fold symmetric components. **A:** Difference of diffraction intensity for positive ( $\Delta t = 600$  ps) and negative delay times at a pump fluence of  $6 \text{ mJ/cm}^2$ . Blue (red) areas indicate reduced (enhanced) intensity. **B, C:** Area of interest for calculating the radial average of the isotropic (B) and the six-fold symmetric (C) components. Regions which are not considered are colored in black or gray (central beam block).

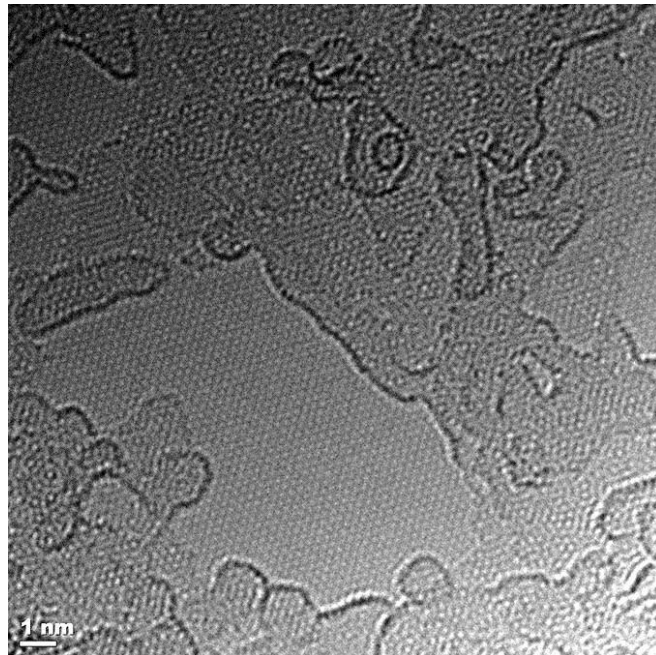


**Fig. S3.** PMMA/graphene bilayer TEM image: High-resolution TEM image of graphene and PMMA layer at 80 keV electron energy. Note that the significant electron dose in this image has already caused polymer degradation.

(Courtesy of Stefanie Strauch, James E. Evans, and Nigel D. Browning. This image is part of the Chemical Imaging Initiative at Pacific Northwest National Laboratory under Contract DE-AC05-76RL01830 operated for DOE by Battelle. A portion of the research was performed using EMSL, a national scientific user facility sponsored by the Department of Energy's Office of Biological and Environmental Research and located at Pacific Northwest National Laboratory.)

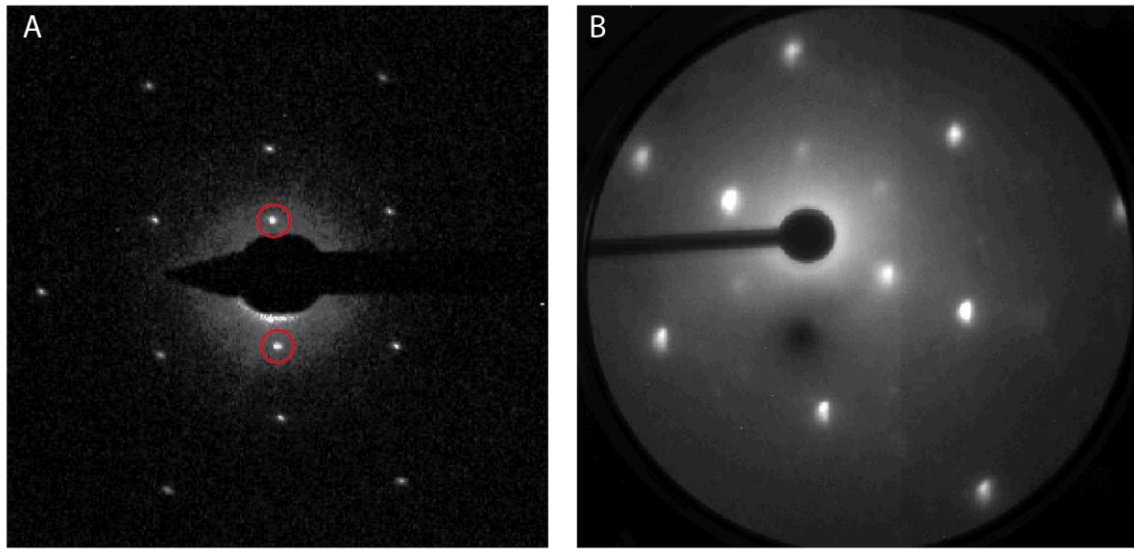


**Fig. S4.** Diffraction images indicating the stripe-like character of the PMMA superstructure. **A:** Low-dose cryo-TEM diffraction pattern (electron probe diameter: few tens of nanometers, 300 keV electron energy) displaying only two PMMA (single domain) diffraction spots (red rings). Image: courtesy of Holger Stark (Max Planck Institute for Biophysical Chemistry). **B:** Transmission ultrafast low-energy electron diffraction image (electron probe diameter: few tens of micrometers, 450 eV electron energy) of a sample region displaying a strongly preferred domain orientation of the PMMA superstructure. This enhances the intensity of two opposing superstructure spots.

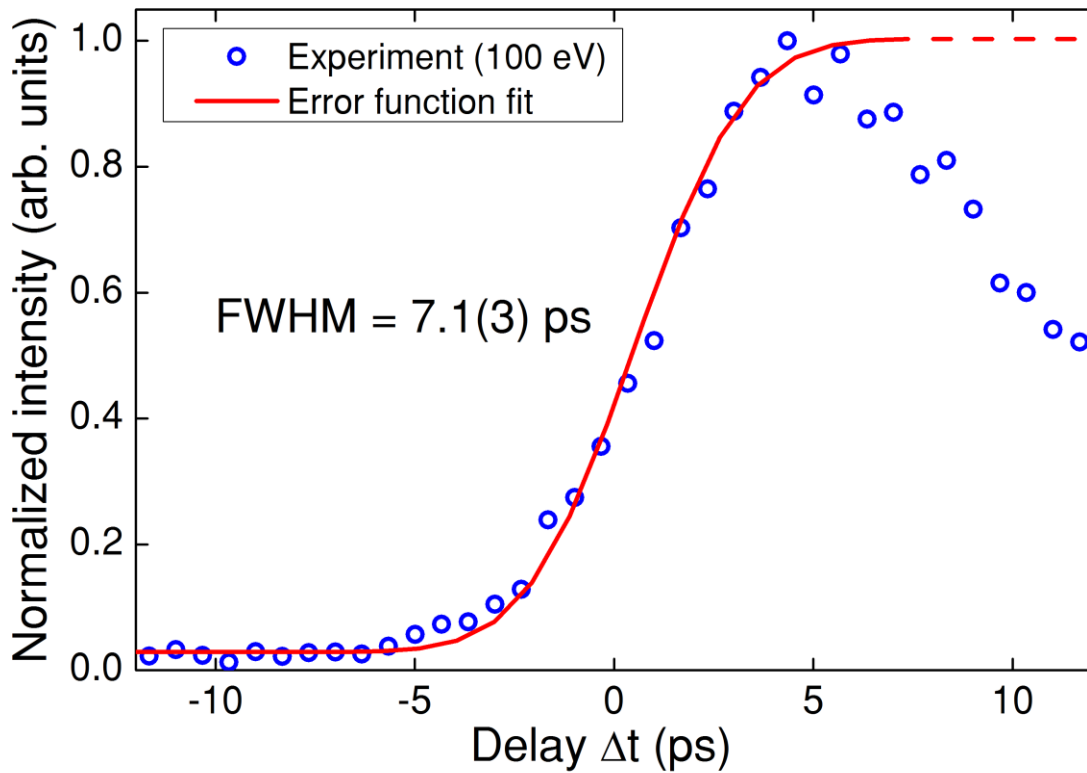


**Fig. S5.** Temporal pulse characterization at low electron energies. Delay-dependent intensity change induced by a transient electric field for a collimated beam at an electron energy of 100 eV (open circles). Red line: Error function adapted to transient intensity change, yielding an electron pulse duration of about 7 ps (FWHM, full-width-at-half-maximum). For a more detailed description of the method and results for high energy electrons, please see Refs. (25, 27, 48).

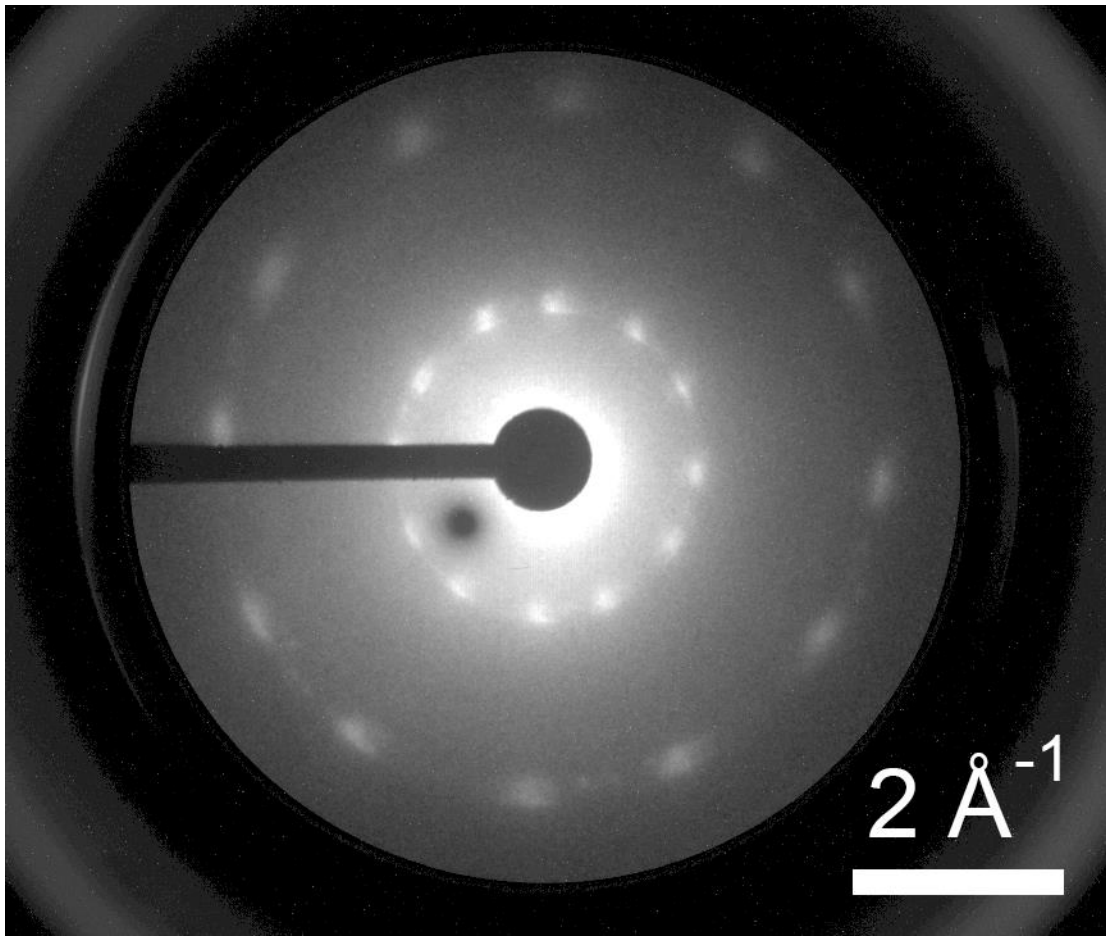


**Fig. S6.** Diffraction image of the polymer/graphene bilayer system recorded at an electron energy of only 150 eV (in transmission), demonstrating the capability of the setup to operate at energies used in conventional low-energy electron diffraction (LEED). The pattern exhibits a 12-fold symmetry, which stems from a superposition of two predominant domain orientations of the graphene substrate rotated by approx. 30° with respect to each other.

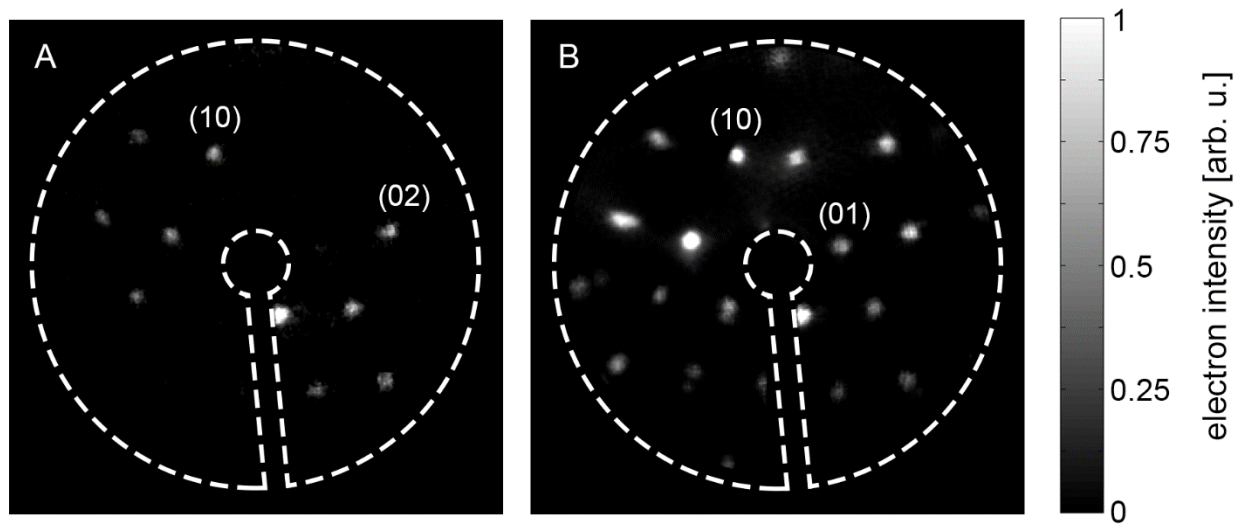


**Fig. S7.** Demonstration of back-reflection LEED with the same laser-triggered electron source as used for the data in the main text. Diffraction images recorded from a single-crystalline sapphire (0001) surface in a reflection geometry using an angle of incidence of  $45^\circ$  at an electron energy of 380 eV (**A**), and averaged between 335 eV and 435 eV (**B**). The weak distortions of the diffraction patterns stem from the planar electron detector placed at an angle of  $90^\circ$  relative to the incident beam.

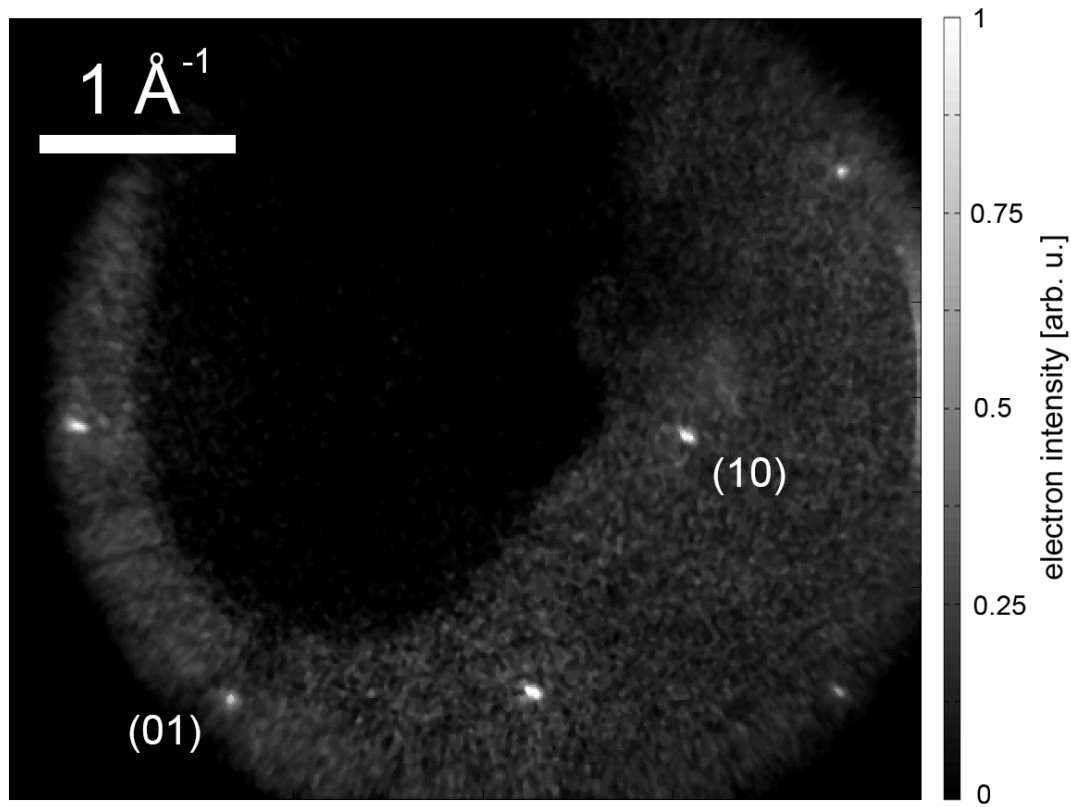


**Fig. S8.** Diffraction image recorded in normal incidence backscattering with a miniaturized laser-triggered electron source (outer diameter: 7 mm). The sample is a single-crystalline sapphire (0001) surface (electron energy: 150 eV). The central dark area corresponds to shadowing by the electron gun in back reflection.

## References

1. S. L. Johnson, E. Vorobeva, P. Beaud, C. J. Milne, G. Ingold, Full reconstruction of a crystal unit cell structure during coherent femtosecond motion. *Phys. Rev. Lett.* **103**, 205501 (2009). [Medline](#) [doi:10.1103/PhysRevLett.103.205501](#)
2. V. Juvé, M. Holtz, F. Zamponi, M. Woerner, T. Elsaesser, A. Borgschulte, Field-driven dynamics of correlated electrons in LiH and NaBH<sub>4</sub> revealed by femtosecond x-ray diffraction. *Phys. Rev. Lett.* **111**, 217401 (2013). [Medline](#) [doi:10.1103/PhysRevLett.111.217401](#)
3. D. M. Fritz, D. A. Reis, B. Adams, R. A. Akre, J. Arthur, C. Blome, P. H. Bucksbaum, A. L. Cavalieri, S. Engemann, S. Fahy, R. W. Falcone, P. H. Fuoss, K. J. Gaffney, M. J. George, J. Hajdu, M. P. Hertlein, P. B. Hillyard, M. Horn-von Hoegen, M. Kammler, J. Kaspar, R. Kienberger, P. Krejcik, S. H. Lee, A. M. Lindenbergs, B. McFarland, D. Meyer, T. Montagne, E. D. Murray, A. J. Nelson, M. Nicoul, R. Pahl, J. Rudati, H. Schlarb, D. P. Siddons, K. Sokolowski-Tinten, T. Tschentscher, D. von der Linde, J. B. Hastings, Ultrafast bond softening in bismuth: Mapping a solid's interatomic potential with X-rays. *Science* **315**, 633–636 (2007). [Medline](#) [doi:10.1126/science.1135009](#)
4. B. J. Siwick, J. R. Dwyer, R. E. Jordan, R. J. D. Miller, An atomic-level view of melting using femtosecond electron diffraction. *Science* **302**, 1382–1385 (2003). [Medline](#) [doi:10.1126/science.1090052](#)
5. P. Baum, D.-S. Yang, A. H. Zewail, 4D visualization of transitional structures in phase transformations by electron diffraction. *Science* **318**, 788–792 (2007). [Medline](#) [doi:10.1126/science.1147724](#)
6. M. Eichberger, H. Schäfer, M. Krumova, M. Beyer, J. Demsar, H. Berger, G. Moriena, G. Sciaiani, R. J. Miller, Snapshots of cooperative atomic motions in the optical suppression of charge density waves. *Nature* **468**, 799–802 (2010). [Medline](#) [doi:10.1038/nature09539](#)
7. A. H. Zewail, Four-dimensional electron microscopy. *Science* **328**, 187–193 (2010). [Medline](#) [doi:10.1126/science.1166135](#)
8. T. LaGrange, G. H. Campbell, B. W. Reed, M. Taheri, J. B. Pesavento, J. S. Kim, N. D. Browning, Nanosecond time-resolved investigations using the in situ of dynamic transmission electron microscope (DTEM). *Ultramicroscopy* **108**, 1441–1449 (2008). [Medline](#) [doi:10.1016/j.ultramic.2008.03.013](#)
9. O. F. Mohammed, D.-S. Yang, S. K. Pal, A. H. Zewail, 4D scanning ultrafast electron microscopy: Visualization of materials surface dynamics. *J. Am. Chem. Soc.* **133**, 7708–7711 (2011). [Medline](#) [doi:10.1021/ja2031322](#)
10. M. Chergui, Picosecond and femtosecond X-ray absorption spectroscopy of molecular systems. *Acta Crystallogr. A* **66**, 229–239 (2010). [Medline](#) [doi:10.1107/S010876730904968X](#)
11. F. Carbone, O.-H. Kwon, A. H. Zewail, Dynamics of chemical bonding mapped by energy-resolved 4D electron microscopy. *Science* **325**, 181–184 (2009). [Medline](#) [doi:10.1126/science.1175005](#)

12. J. M. Kosterlitz, D. J. Thouless, Ordering, metastability and phase transitions in two-dimensional systems. *J. Phys. Chem.* **6**, 1181–1203 (1973).
13. P. M. Chaikin, T. C. Lubensky, *Principles of Condensed Matter Physics* (Cambridge University Press, Cambridge, 2000).
14. A. Hanisch-Blicharski, A. Janzen, B. Krenzer, S. Wall, F. Klasing, A. Kalus, T. Frigge, M. Kammler, M. Horn-von Hoegen, Ultra-fast electron diffraction at surfaces: From nanoscale heat transport to driven phase transitions. *Ultramicroscopy* **127**, 2–8 (2013). [Medline doi:10.1016/j.ultramic.2012.07.017](#)
15. M. A. Van Hove, W. H. Weinberg, C.-M. Chan, *Low-Energy Electron Diffraction* (Springer, Berlin Heidelberg, 1986).
16. S. Schäfer, W. Liang, A. H. Zewail, Structural dynamics of surfaces by ultrafast electron crystallography: Experimental and multiple scattering theory. *J. Chem. Phys.* **135**, 214201 (2011). [Medline doi:10.1063/1.3663963](#)
17. R. S. Becker, G. S. Higashi, J. A. Golovchenko, Low-energy electron diffraction during pulsed laser annealing: A time-resolved surface structural study. *Phys. Rev. Lett.* **52**, 307–310 (1984). [doi:10.1103/PhysRevLett.52.307](#)
18. C. Cirelli, M. Hengsberger, A. Dolocan, H. Over, J. Osterwalder, T. Greber, Direct observation of space charge dynamics by picosecond low-energy electron scattering. *Europhys. Lett.* **85**, 17010 (2009). [doi:10.1209/0295-5075/85/17010](#)
19. R. Karrer, H. J. Neff, M. Hengsberger, T. Greber, J. Osterwalder, Design of a miniature picosecond low-energy electron gun for time-resolved scattering experiments. *Rev. Sci. Instrum.* **72**, 4404 (2001). [doi:10.1063/1.1419219](#)
20. M. Krüger, M. Schenk, P. Hommelhoff, Attosecond control of electrons emitted from a nanoscale metal tip. *Nature* **475**, 78–81 (2011). [Medline doi:10.1038/nature10196](#)
21. G. Herink, D. R. Solli, M. Gulde, C. Ropers, Field-driven photoemission from nanostructures quenches the quiver motion. *Nature* **483**, 190–193 (2012). [Medline doi:10.1038/nature10878](#)
22. A. Paarmann, M. Gulde, M. Müller, S. Schäfer, S. Schweda, M. Maiti, C. Xu, T. Hohage, F. Schenk, C. Ropers, R. Ernstorfer, Coherent femtosecond low-energy single-electron pulses for time-resolved diffraction and imaging: A numerical study. *J. Appl. Phys.* **112**, 113109 (2012). [doi:10.1063/1.4768204](#)
23. E. Quinonez, J. Handali, B. Barwick, Femtosecond photoelectron point projection microscope. *Rev. Sci. Instrum.* **84**, 103710 (2013). [Medline doi:10.1063/1.4827035](#)
24. J. C. H. Spence, T. Vecchione, U. Weierstall, A coherent photofield electron source for fast diffractive and point-projection imaging. *Philos. Mag.* **90**, 4691–4702 (2010). [doi:10.1080/14786431003630868](#)
25. H. Park, J. M. Zuo, Direct measurement of transient electric fields induced by ultrafast pulsed laser irradiation of silicon. *Appl. Phys. Lett.* **94**, 251103 (2009). [doi:10.1063/1.3157270](#)
26. Materials and methods are available as supplementary materials on *Science Online*.

27. R. K. Raman, Z. Tao, T.-R. Han, C.-Y. Ruan, Ultrafast imaging of photoelectron packets generated from graphite surface. *Appl. Phys. Lett.* **95**, 181108 (2009). [doi:10.1063/1.3259779](https://doi.org/10.1063/1.3259779)
28. M. Tress, E. U. Mapesa, W. Kossack, W. K. Kipnusu, M. Reiche, F. Kremer, Glassy dynamics in condensed isolated polymer chains. *Science* **341**, 1371–1374 (2013). [Medline doi:10.1126/science.1238950](https://doi.org/10.1126/science.1238950)
29. J. A. Forrest, K. Dalnoki-Veress, The glass transition in thin polymer films. *Adv. Colloid Interfac.* **94**, 167–195 (2001). [doi:10.1016/S0001-8686\(01\)00060-4](https://doi.org/10.1016/S0001-8686(01)00060-4)
30. O. M. Braun, Y. S. Kivshar, *The Frenkel-Kontorova Model: Concepts, Methods, and Applications* (Springer, Berlin Heidelberg, 2004).
31. A. N. Rissanou, V. Harmandaris, Structure and dynamics of poly(methyl methacrylate)/graphene systems through atomistic molecular dynamics simulations. *J. Nanopart. Res.* **15**, 1589 (2013). [doi:10.1007/s11051-013-1589-2](https://doi.org/10.1007/s11051-013-1589-2)
32. Y.-C. Lin, C. C. Lu, C. H. Yeh, C. Jin, K. Suenaga, P. W. Chiu, Graphene annealing: How clean can it be? *Nano Lett.* **12**, 414–419 (2012). [Medline doi:10.1021/nl203733r](https://doi.org/10.1021/nl203733r)
33. A. K. Geim, I. V. Grigorieva, Van der Waals heterostructures. *Nature* **499**, 419–425 (2013). [Medline doi:10.1038/nature12385](https://doi.org/10.1038/nature12385)
34. J. Kumaki, T. Kawauchi, E. Yashima, Two-dimensional folded chain crystals of a synthetic polymer in a Langmuir–Blodgett film. *J. Am. Chem. Soc.* **127**, 5788–5789 (2005). [Medline doi:10.1021/ja050457e](https://doi.org/10.1021/ja050457e)
35. J. S. Ha *et al.*, Structural study of a poly(methylmethacrylate) Langmuir–Blodgett film on a graphite surface by scanning tunneling microscope. *J. Vac. Sci. Technol. B* **12**, 1977–1980 (1994). [doi:10.1116/1.587683](https://doi.org/10.1116/1.587683)
36. Whereas the (10) diffraction spot of PMMA overlaps with that of graphene, the (3/2 0) PMMA spot is not observed, which is most likely a result of the chain form factor or disorder.
37. A. Reina, X. Jia, J. Ho, D. Nezich, H. Son, V. Bulovic, M. S. Dresselhaus, J. Kong, Large area, few-layer graphene films on arbitrary substrates by chemical vapor deposition. *Nano Lett.* **9**, 30–35 (2009). [Medline doi:10.1021/nl801827v](https://doi.org/10.1021/nl801827v)
38. Y. Takanashi, J. Kumaki, Significant melting point depression of two-dimensional folded-chain crystals of isotactic poly(methyl methacrylate)s observed by high-resolution *in situ* atomic force microscopy. *J. Phys. Chem. B* **117**, 5594–5605 (2013). [Medline doi:10.1021/jp401284t](https://doi.org/10.1021/jp401284t)
39. See, e.g., (40). In the measurements presented, the total dose on a given sample position was limited to minimize degradation effects on the observed structural dynamics. This was achieved by restricting the integration time and number of delay times measured.
40. D. T. Grubb, Radiation damage and electron microscopy of organic polymers. *J. Mater. Sci.* **9**, 1715–1736 (1974). [doi:10.1007/BF00540772](https://doi.org/10.1007/BF00540772)

41. R. R. Nair, P. Blake, A. N. Grigorenko, K. S. Novoselov, T. J. Booth, T. Stauber, N. M. Peres, A. K. Geim, Fine structure constant defines visual transparency of graphene. *Science* **320**, 1308 (2008). [Medline doi:10.1126/science.1156965](#)
42. E. Pop, V. Varshney, A. K. Roy, Thermal properties of graphene: Fundamentals and applications. *MRS Bull.* **37**, 1273–1281 (2012). [doi:10.1557/mrs.2012.203](#)
43. D. R. Stull, H. Prophet, *National Standard Reference Data Series, NBS-37* (U.S. National Bureau of Standards, Washington, DC, 1971).
44. J. Brandrup, E. H. Immergut, E. A. Grulke, *Polymer Handbook* (Wiley, New York, 1999).
45. B. Krenzer, A. Hanisch-Blicharski, P. Schneider, T. Payer, S. Möllenbeck, O. Osmani, M. Kammler, R. Meyer, M. Horn-von Hoegen, Phonon confinement effects in ultrathin epitaxial bismuth films on silicon studied by time-resolved electron diffraction. *Phys. Rev. B* **80**, 024307 (2009). [doi:10.1103/PhysRevB.80.024307](#)
46. S. Hida, T. Hori, T. Shiga, J. Elliott, J. Shiomi, Thermal resistance and phonon scattering at the interface between carbon nanotube and amorphous polyethylene. *Int. J. Heat Mass Transfer* **67**, 1024–1029 (2013). [doi:10.1016/j.ijheatmasstransfer.2013.08.068](#)
47. S. T. Huxtable, D. G. Cahill, S. Shenogin, L. Xue, R. Ozisik, P. Barone, M. Usrey, M. S. Strano, G. Siddons, M. Shim, P. Kebinski, Interfacial heat flow in carbon nanotube suspensions. *Nat. Mater.* **2**, 731–734 (2003). [Medline doi:10.1038/nmat996](#)
48. G. F. Mancini, B. Mansart, S. Pagano, B. van der Geer, M. de Loos, F. Carbone, Design and implementation of a flexible beamline for fs electron diffraction experiments. *Nuc. Inst. Meth. Phys. A* **691**, 113–122 (2012). [doi:10.1016/j.nima.2012.06.057](#)